

RESEARCH LETTER

10.1029/2017GL076968

Key Points:

- Globally, atmospheric rivers (ARs) are ~10% fewer, ~25% longer, ~25% wider, and with stronger moisture transport under the RCP8.5 scenario
- In the midlatitudes where ARs are most frequent, AR conditions are ~50–60% more frequent and AR transport is ~20% stronger in the future
- Systematic low biases exist in the midlatitudes in historical AR frequency (~10%), zonal (~15%), and meridional (~25%) moisture transport

Supporting Information:

- Supporting Information S1

Correspondence to:

D. E. Waliser,
 duane.e.waliser@jpl.nasa.gov

Citation:

Espinoza, V., Waliser, D. E., Guan, B., Lavers, D. A., & Ralph, F. M. (2018). Global analysis of climate change projection effects on atmospheric rivers. *Geophysical Research Letters*, 45, 4299–4308. <https://doi.org/10.1029/2017GL076968>

Received 26 JUL 2017

Accepted 10 APR 2018

Accepted article online 19 APR 2018

Published online 7 MAY 2018

Global Analysis of Climate Change Projection Effects on Atmospheric Rivers

Vicky Espinoza^{1,2} , Duane E. Waliser² , Bin Guan^{2,3} , David A. Lavers⁴ ,
 and F. Martin Ralph⁵ 

¹Sonny Astani Civil and Environmental Engineering Department, University of Southern California, Los Angeles, CA, USA, ²Jet Propulsion Laboratory, California Institute of Technology, Pasadena, CA, USA, ³Joint Institute for Regional Earth System Science and Engineering, University of California, Los Angeles, CA, USA, ⁴European Centre for Medium-Range Weather Forecasts, Reading, UK, ⁵Center for Western Weather and Water Extremes, Scripps Institution of Oceanography at University of California, San Diego, CA, USA

Abstract A uniform, global approach is used to quantify how atmospheric rivers (ARs) change between Coupled Model Intercomparison Project Phase 5 historical simulations and future projections under the Representative Concentration Pathway (RCP) 4.5 and RCP8.5 warming scenarios. The projections indicate that while there will be ~10% fewer ARs in the future, the ARs will be ~25% longer, ~25% wider, and exhibit stronger integrated water vapor transports (IVTs) under RCP8.5. These changes result in pronounced increases in the frequency (IVT strength) of AR conditions under RCP8.5: ~50% (25%) globally, ~50% (20%) in the northern midlatitudes, and ~60% (20%) in the southern midlatitudes. The models exhibit systematic low biases across the midlatitudes in replicating historical AR frequency (~10%), zonal IVT (~15%), and meridional IVT (~25%), with sizable intermodel differences. A more detailed examination of six regions strongly impacted by ARs suggests that the western United States, northwestern Europe, and southwestern South America exhibit considerable intermodel differences in projected changes in ARs.

Plain Language Summary Atmospheric rivers (ARs) are elongated strands of horizontal water vapor transport, accounting for over 90% of the poleward water vapor transport across midlatitudes. These “rivers in the sky” have important implications for extreme precipitation when they make landfall, particularly along the west coasts of many midlatitude continents (e.g., North America, South America, and West Europe) due to orographic lifting. ARs are important contributors to extreme weather and precipitation events, and while their presence can contribute to beneficial rainfall and snowfall, which can mitigate droughts, they can also lead to flooding and extreme winds. This study takes a uniform, global approach that is used to quantify how ARs change between Coupled Model Intercomparison Project Phase 5 historical simulations and future projections under the Representative Concentration Pathway (RCP) 4.5 and RCP8.5 warming scenarios globally. The projections indicate that while there will be ~10% fewer ARs in the future, the ARs will be ~25% longer, ~25% wider, and exhibit stronger integrated water vapor transports under RCP8.5. These changes result in pronounced increases in the frequency (integrated water vapor transport strength) of AR conditions under RCP8.5: ~50% (25%) globally, ~50% (20%) in the northern midlatitudes, and ~60% (20%) in the southern midlatitudes.

1. Introduction

Atmospheric rivers (ARs) are elongated strands of horizontal water vapor transport, accounting for over 90% of the poleward water vapor transport across midlatitudes (Zhu & Newell, 1998). These “rivers in the sky” have important implications for extreme precipitation when they make landfall, particularly along the west coasts of many midlatitude continents (e.g., North America, South America, and western Europe) and especially when encountering orographic lifting (e.g., Neiman et al., 2009; Ralph et al., 2004). ARs are important contributors to extreme weather and precipitation events, and while their presence can contribute to beneficial rainfall and snowfall (Dettinger et al., 2011; Guan et al., 2010), which can mitigate droughts (Dettinger, 2013), they can also lead to flooding (e.g., Lavers et al., 2011; Leung & Qian, 2009; Neiman et al., 2011; Ralph et al., 2006, 2013; Ralph & Dettinger, 2011) and extreme winds (Waliser & Guan, 2017). These important impacts have motivated a number of climate change studies on ARs, with studies to date focusing mainly only on the west coasts of North America (Dettinger, 2011; Gao et al., 2015; Hagos et al., 2016; Payne &

Table 1

Comparison of Mean Changes in AR Frequency (Percent of Time Steps) and IVT ($\text{kg} \cdot \text{m}^{-1} \cdot \text{s}^{-1}$) Between the Current Study and Previous Studies for the Western U.S. and Western Europe

Publication	Historical period	Projection period	Geographic region	AR Freq (\pm %)	AR IVT (\pm %)
Dettinger (2011)	1961–2000	2046–2065; 2081–2100	CA Coast	+30	+10
Pierce et al. (2013)	1985–1994	2060s	CA Coast	+25–100	--
Warner et al. (2015)	1970–1999	2070–2099	U.S. West Coast	+230–290	+30
Payne and Magnusdottir (2015)	1980–2005	2070–2100	U.S. West Coast	+23–35	--
Gao et al. (2015)	1975–2004	2070–2099	U.S. West Coast	+50–600	--
Hagos et al. (2016)	1920–2005	2006–2099	U.S. West Coast	+35	--
Shields and Kiehl (2016a)	1960–2005	2055–2100	U.S. West Coast	+8	--
Espinoza et al. (2018, current study)	1979–2002	2073–2096	U.S. West Coast	+45	+30
<i>Lavers et al. (2013)</i>	<i>1980–2005</i>	<i>2074–2099</i>	<i>W. Europe</i>	<i>+50–100</i>	<i>--</i>
<i>Gao et al. (2016)</i>	<i>1975–2004</i>	<i>2070–2099</i>	<i>W. Europe</i>	<i>+127–275</i>	<i>+20–50</i>
<i>Ramos et al. (2016)</i>	<i>1980–2005</i>	<i>2074–2099</i>	<i>Europe</i>	<i>+100–300</i>	<i>+30</i>
<i>Shields and Kiehl (2016a)</i>	<i>1960–2005</i>	<i>2055–2100</i>	<i>North Atlantic</i>	<i>+4</i>	<i>--</i>
<i>Espinoza et al. (2018, current study)</i>	<i>1979–2002</i>	<i>2073–2096</i>	<i>W. Europe</i>	<i>+60</i>	<i>+30</i>

Note. The bold (italic) region is previous studies focusing on the U.S. West Coast (western Europe). The studies are ordered from oldest to most recent within each geographic region (bold and italic). Note that each of the studies mentioned above differ in their methodologies, models used, and their study periods limiting their comparability.

Magnusdottir, 2015; Pierce et al., 2013; Radić et al., 2015; Shields & Kiehl, 2016a, 2016b; Warner et al., 2015) and Europe (Gao et al., 2016; Lavers et al., 2013; Ramos et al., 2016; Shields & Kiehl, 2016a).

The first climate change study on ARs was conducted by Dettinger (2011) and focused on landfalling ARs in California using seven Coupled Model Intercomparison Project (CMIP) Phase 3 models with the A2 greenhouse-gas emissions scenario. This study found AR frequency increases of about 30% depending on the model by the end of the 21st century and noted increases in storm temperature, length of AR season, and peak AR intensity values. Note that climate change studies on ARs have generally defined AR frequency as the fraction of days a particular grid point has an AR detected over it. Warner et al. (2015) extended the consideration to a larger area along the west coast of North America using 10 CMIP5 (Taylor et al., 2012) models for a historical period (1970–1999) and projection period (2070–2099) for the Representative Concentration Pathway (RCP) 8.5 warming scenario. This study conducted a multi-model mean (MMM) analysis with results indicating ~230–290% increase in AR days. The analysis also showed that there would be an increase in extreme values of integrated water vapor transport (IVT) magnitude and IWV of ~30%. Precipitation values for the MMM showed ~15–39% increase. Using more CMIP5 models (a total of 24), Gao et al. (2015) indicated an ~50–600% increase in AR days under RCP8.5, depending on the season and landfall location along western North America. Another study by Payne and Magnusdottir (2015) using 28 CMIP5 models found 23–35% increases in projected AR landfall dates in this region under RCP8.5. Hagos et al. (2016) showed increases in projected AR landfall days by 35% under RCP8.5 based on a 29-member ensemble of the National Center for Atmospheric Research Community Earth System Model. Other studies have also examined projected AR changes in western North America, as summarized in Table 1.

For the European region, Lavers et al. (2013) used five CMIP5 models, comparing historical (1980–2005) and projection (2074–2099) periods for the RCP4.5 and RCP8.5 scenarios. This study also used an IVT-based threshold approach for detecting ARs. This study found that AR frequency approximately doubled in Britain under RCP8.5 and determined that the change was dominated by the thermodynamic (moistening) response to warming rather than from the influence of wind changes. Gao et al. (2016) conducted a study with a focus on comparing the influences of thermodynamic and dynamic effects on ARs and the quantification of the number of AR days across the European sector. By using 24 CMIP5 models, this study found that AR frequency increased by ~127–275% by the end of the century under RCP8.5. Not only did the study find that the projected increases in AR frequency were influenced by thermodynamic processes but found that variability in wind speed and direction related to shifts in the midlatitude jet stream played a dominant role in the changes of ARs in the European sector. Other studies have also examined projected AR changes in Europe, as summarized in Table 1.

While all the studies discussed and cited above have tended toward the same general conclusions (Table 1), that is, finding an increase in AR frequency and IVT, they have been limited to two regions in the Northern Hemisphere. A uniform global assessment of climate change impacts on ARs has not been performed despite the global presence and impacts of ARs (Guan & Waliser, 2015; Waliser et al., 2012; Waliser & Guan, 2017; Zhu & Newell, 1998). For example, despite the number of studies performed on western North America and western Europe, the differences in data sets and methodologies used make it challenging to use these studies to compare impacts of climate change effects on ARs in these two regions. This study addresses this research gap by analyzing climate change impacts on AR frequencies and IVT using a globally consistent approach on historical climate simulations and future projections of climate change from CMIP5.

2. Models and Methodology

2.1. CMIP5 Model Data

IVT values were constructed from daily values of 3-D wind and water vapor model outputs at four pressure levels between 500 and 1,000 hPa inclusive, namely, the data described in Lavers et al. (2015; their Table S1). We used 21 out of the 22 models examined in that study because the IVT data for one model were not available at the time of this analysis. The horizontal resolution of the models ranges from 1.125° to 2.813°. The study periods were 1979–2002 from the historical simulations and 2073–2096 from the RCP4.5 and RCP8.5 scenarios, determined as a time frame that contains the maximum number of overlapping years among all the models and one that spans the same number of years for the historical and the two RCP runs. The more stringent requirement on the consistency in data set period resulted in three fewer years included for analysis relative to Lavers et al. (2015).

2.2. AR Global Detection Algorithm

The AR global detection algorithm introduced in Guan and Waliser (2015) was used. Notable AR criteria used in the algorithm include IVT magnitude at each grid cell within a contiguous region (“object”) being above the 85th percentile for that grid cell and season, the length of the object being greater than 2000 km, and the length-to-width ratio greater than 2. For a given model, AR detection for the historical simulation and future projections (RCP4.5 and RCP8.5) are all based on the IVT 85th percentile derived from the historical simulation. AR detection and subsequent calculation of AR frequency and IVT are based on the respective horizontal resolution of each individual model. Regridding to a common grid is done only when calculating the multimodel ensemble mean. It is expected that the inherent differences between different models are much larger than the sensitivity of the results to the choice of horizontal resolution used for AR detection and subsequent calculations (e.g., Guan & Waliser, 2017). In that regard, the step at which regridding is introduced into the calculations (e.g., before or after AR detection) is not an important consideration in the current analysis. AR detection results based on the Guan and Waliser (2015) algorithm was found to be consistent with regional AR detection methods developed for western North America (Neiman et al., 2008), Britain (Lavers et al., 2011), and East Antarctica (Gorodetskaya et al., 2014), with over ~90% agreement in detected AR landfall dates.

2.3. AR Frequency and IVT Analysis

The AR frequency is calculated as the number of AR days detected at each grid cell for the given historical or future projection period normalized by the total number of days in the given period. Mean AR IVT at each grid cell is based on averaging the IVT values over the days detected as ARs. Once AR frequency and IVT have been computed for each individual model, they are (bi-linearly) interpolated to a common 1.5° × 1.5° grid (which matches the grid of the ERA-Interim reanalysis used as the observational reference) to create MMM maps.

To illustrate the calculation procedures, a set of histograms, shown in Figure 1a, are created for a single location in the southeast Pacific Ocean (61°S, 216.25°E) from the Geophysical Fluid Dynamics Laboratory Coupled Model 3 (GFDL-CM3) model simulations. The red (blue) histogram includes all IVT values at that point for the historical (RCP8.5 projection) period. The number of IVT values sampled in each histogram is shown in the plot’s legend. Additional histograms delineate the IVT values of the detected ARs for the historical (pink) and RCP8.5 (light blue) simulations—with both using the IVT 85th percentile derived from the historical period for detecting ARs. For this location and model, the histograms show that the RCP8.5 scenario results in a significant increase (~140%) in the number of AR days given the historical IVT threshold. An additional

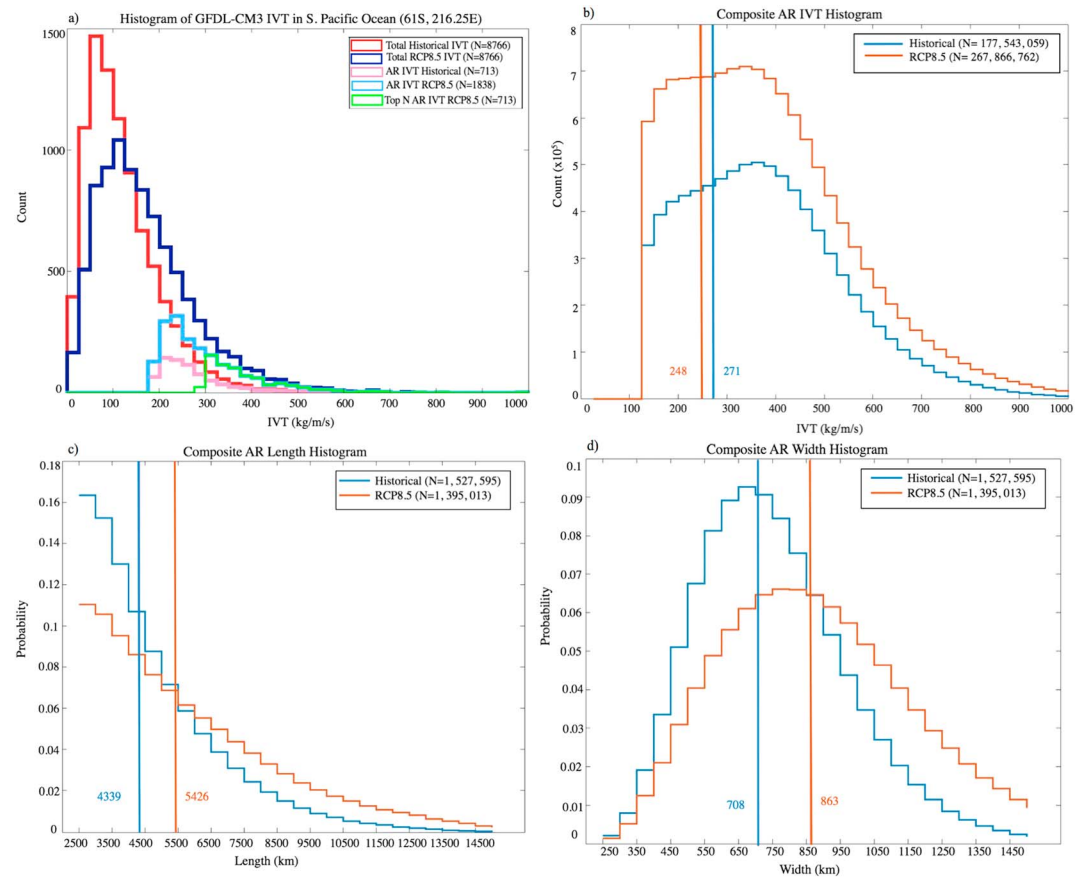


Figure 1. (a) Histograms of IVT values ($\text{kg} \cdot \text{m}^{-1} \cdot \text{s}^{-1}$) at a single grid point (61°S , 216.25°E) in the South Pacific Ocean from the GFDL-CM3 simulations. The red (dark blue) histogram includes all (i.e., both AR and non-AR grid cells) IVT values for the historical period, that is, 1979–2002 (RCP8.5 period, i.e., 2073–2096). The pink (light blue) histogram includes the IVT values associated with only AR events in the historical period (AR events in the RCP8.5 scenario based on the AR IVT threshold from the historical period). The green histogram includes the top N AR IVT values for the RCP8.5 scenario, where N is determined by number of AR events from the historical simulation (i.e., 713). Thus, the number of IVT values contributing to the pink and green histograms is the same. Multimodel ensemble histograms of (b) IVT values at each grid cell within the ARs, (c) AR lengths (km), and (d) AR widths (km) for the historical (blue) and RCP8.5 (orange) simulations, with vertical bars representing the overall mean. N values in (b) are the total number of AR grid cells; N values in (c) and (d) are the total number of AR objects.

histogram (green) shows the top N AR IVT values from the RCP8.5, where N is determined by the number of AR days in the historical simulation; thus, the pink and green histograms have the same number of AR IVT values.

The AR frequency results discussed in section 3 (e.g., shadings in Figure 2) are essentially referring to AR frequencies as represented by the light blue and pink histograms. The AR IVT values discussed below (e.g., vectors in Figure 2) are based on averages of the IVT values within the pink and green histograms. Thus, the mean AR IVT to be compared below between the historical and future scenarios is based on averaging over the same number of the most extreme IVT values from each simulation.

3. Results

3.1. Historical Simulations

AR frequency and IVT for the historical, RCP4.5 and RCP8.5 simulations are shown in Figure 2. Also shown is the ERA-Interim AR frequency and IVT for 1979–2002 (Figure 2a; cf. Guan & Waliser, 2015) as the observational

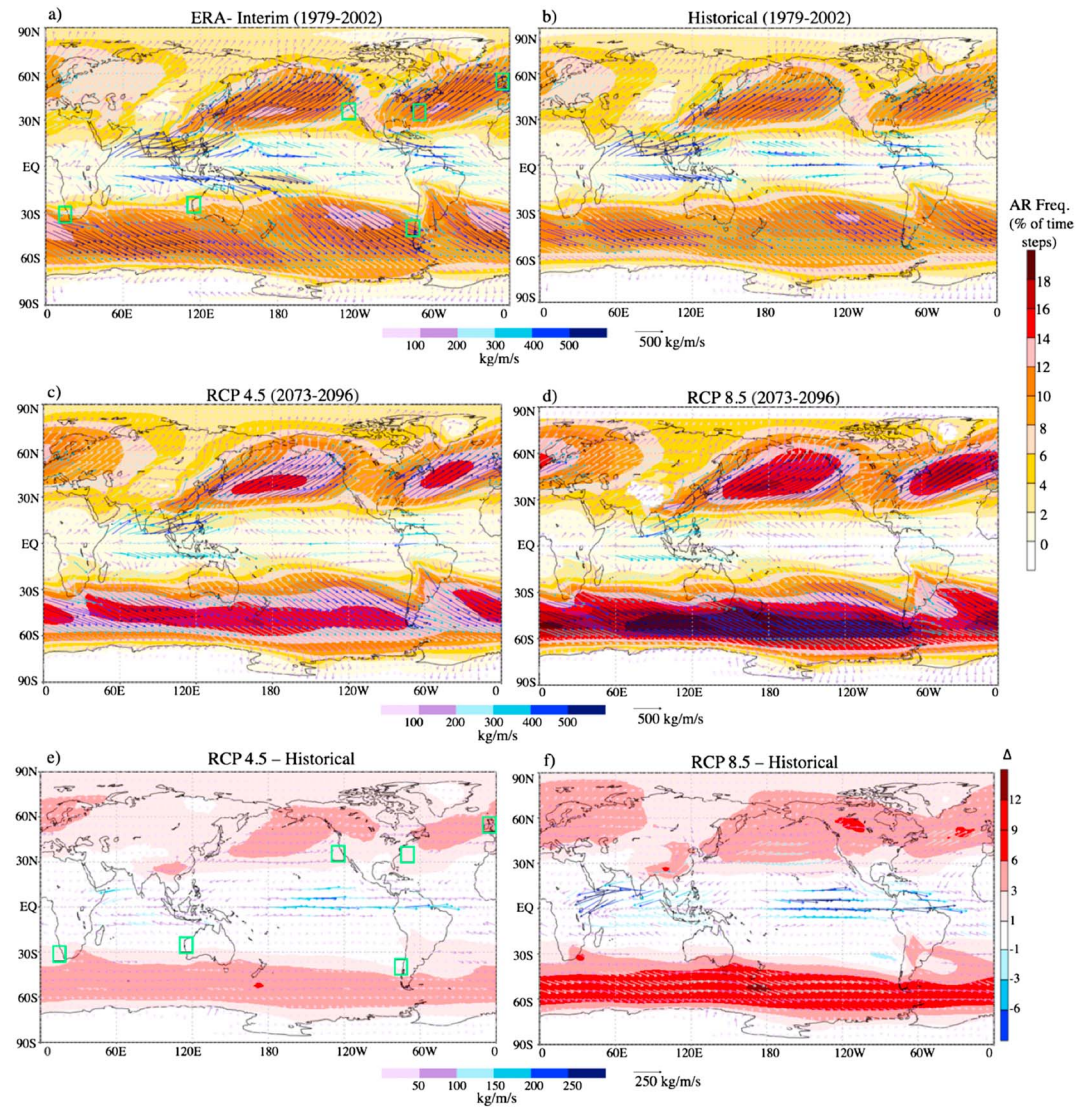


Figure 2. AR frequency (shading; percent of time steps) and IVT (vectors; $\text{kg} \cdot \text{m}^{-1} \cdot \text{s}^{-1}$) for (a) ERA-Interim reanalysis for the historical period (1979–2002) with six green boxes depicting regions analyzed in Figures S2 and S3, (b) the MMM for the 21 CMIP5 models analyzed in this study for the historical period (1979–2002), (c) RCP4.5 warming scenario (2073–2096), and (d) RCP8.5 warming scenario (2073–2096), (e) the difference between (c) and (b) with six green boxes depicting regions analyzed in Figures S2 and S3, and (f) the difference between (d) and (b). Vector magnitudes are indicated by both their length and their color based on the blue color bar.

reference. Comparing Figures 2a and 2b shows that the MMM is a good representation of the observational reference. For AR frequency, and zonal and meridional IVT components, the spatial correlations (root mean square error) between the historical simulation and the reference are 0.98, 0.93, and 0.97 (0.93%, 93.14 $\text{kg} \cdot \text{m}^{-1} \cdot \text{s}^{-1}$, and 51.79 $\text{kg} \cdot \text{m}^{-1} \cdot \text{s}^{-1}$), respectively. The good quantitative agreement between Figures 2a and 2b mainly stems from the MMM capturing the strong latitudinal dependence of the AR frequency and IVT values and the dominant zonal asymmetries of the midlatitude patterns (see red and blue lines in Figures 3c, 3f, and 3i). Direct comparison of the MMM with ERA-Interim shows that the AR frequencies are generally biased low by $\sim 10\%$ in midlatitude regions, with zonal (meridional) IVT biased low by $\sim 15\%$ (25%), particularly in the Southern Ocean. The relatively good MMM representations of AR frequency and IVT provide some confidence to now consider the MMM projected changes in AR frequency and IVT (section 3.2). Subsequent to that will be a discussion of the intermodel differences in historical simulation biases (section 3.3) and projected changes (section 3.4) in AR frequency and IVT.

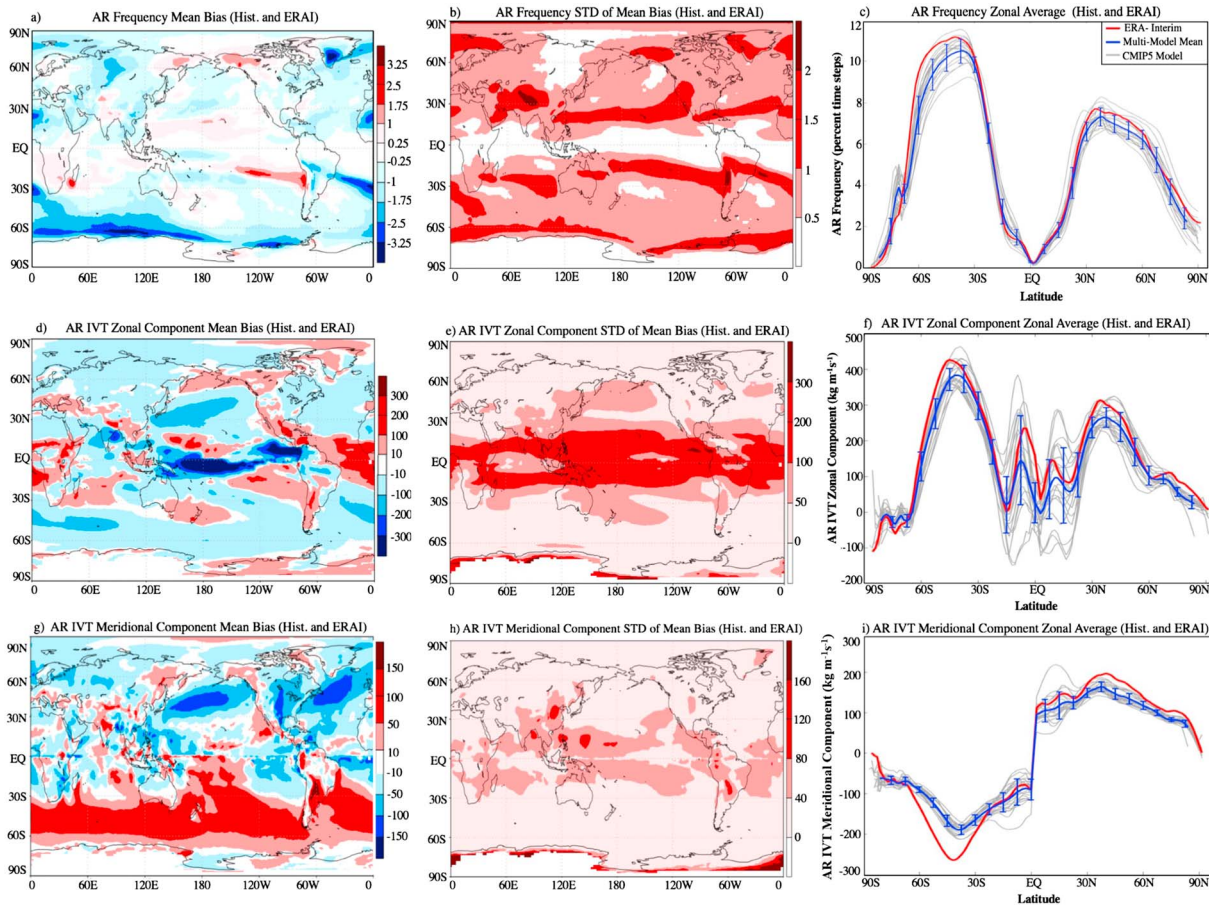


Figure 3. (a) Multimodel mean (MMM) of the individual model biases in AR frequency (percent of time steps) relative to ERA-Interim. (b) Intermodel standard deviation (STD) of the individual model biases around the MMM bias in AR frequency. (c) Zonally averaged AR frequency for individual models (grey), the MMM with standard error of mean (blue), and ERA-Interim (red). (d–f) As (a)–(c) but for AR zonal IVT ($\text{kg} \cdot \text{m}^{-1} \cdot \text{s}^{-1}$). (g–i) As (a)–(c) but for AR meridional IVT ($\text{kg} \cdot \text{m}^{-1} \cdot \text{s}^{-1}$). The errors bars in (c), (f), and (i) represent the standard errors of the MMM.

3.2. Future Projections

Figures 2c and 2d illustrate the MMM AR frequency and IVT values for the RCP4.5 and RCP8.5 simulation. For the RCP8.5 warming scenario, the global mean AR frequency and IVT increase by 49% and 23%, respectively. Most evident is the considerable increase in AR frequency in the midlatitudes, with values, for example, along the Southern Ocean (i.e., 30–60°S area average) rising from around 6–12% for the historical simulations to 12–16% and 14–20% for the RCP4.5 and RCP8.5 simulations, respectively. For the North Pacific (i.e., 30–60°N, 120–240° area average) and North Atlantic (i.e., 30–60°N, 270–360° area average), the AR frequency changes from around 10–12% for the historical simulations to 14–16% and 16–18% for the RCP4.5 and RCP8.5 simulations, respectively. Similarly, there are marked increases in IVT magnitude. For example, IVT values in the North Pacific and North Atlantic, rise from about $350 \text{ kg} \cdot \text{m}^{-1} \cdot \text{s}^{-1}$ in the historical simulation to about $420 \text{ kg} \cdot \text{m}^{-1} \cdot \text{s}^{-1}$ for RCP8.5 scenario. In the Southern Ocean, the IVT values change from 364 to $434 \text{ kg} \cdot \text{m}^{-1} \cdot \text{s}^{-1}$ between the historical and RCP8.5 simulations.

Figures 2e and 2f show the changes between the RCP4.5 and RCP8.5 warming scenarios and the historical simulation, respectively. Referring to the histograms in Figure 1a (see section 2.3), the AR frequency differences in Figure 2f refer to the differences between the example pink and light blue histograms. The IVT differences refer to the differences in the average IVT between the events associated with the green (i.e., RCP8.5) and pink (i.e., historical) histograms. These difference maps indicate AR frequency increases by ~50% globally, ~60% in the Southern Ocean, and ~50% in the Northern Hemisphere (Figure 2f). Moreover, in these same regions, the mean magnitude (in terms of IVT of the strongest of events) increases by 25% globally and by 20% in the northern and southern mid-and-high latitudes for RCP8.5 (Figure 2f). There are

also considerable increases in eastward (westward) tropical AR IVT in the eastern Pacific (Indian) Oceans—although the frequency of ARs is very low in the tropics. Comparing these results with earlier studies on western North America and western Europe (Table 1) shows that these increases are similar, albeit more moderate in a number of cases, to previous studies. It is noted that the different detection and analysis methods used across these earlier studies make it difficult to compare them, and the uniform approach used here not only highlights areas not previously considered but also allows more judicious comparison across different regions.

Figures 1b to 1d highlight additional aggregate measures of projected changes in future AR characteristics. Figure 1b shows model ensemble average histograms of the AR IVT values from the historical and RCP8.5 simulations. Consistent with the increases in AR frequency in Figure 2f is the overall increase in the number of values across the range of IVT, and importantly the approximate doubling of extreme AR IVT events. The model ensemble average histograms of AR lengths and AR widths in Figures 1c and 1d illustrate that these increases in the frequency of AR conditions in Figures 1b and 2f arise from an increase of ~25% in both the lengths and widths of future ARs, despite an ~10% reduction in the number of ARs in the future under the RCP8.5 scenario (see Figures 1c and 1d legend).

3.3. Intermodel Differences in Historical Simulations

As a means to consider model fidelity and projection uncertainty, we illustrate and discuss intermodel differences against the observational reference and among the projections. Figure 3 summarizes comparisons between the historical simulations and the ERA-Interim observed reference values for AR frequency, zonal IVT, and meridional IVT (rows 1, 2, and 3, respectively). In each row, the left (middle) map shows the MMM (standard deviation) of the individual model biases. The right map shows the zonal averages of AR frequency or IVT for each individual model, the MMM, and the ERA-Interim reanalysis. For AR frequency, the figure shows little systematic bias across the model ensemble (Figure 3a), although rather significant disagreement in the subtropics are found (Figures 3b and 3c) as in Payne and Magnusdottir (2015) for ARs in the northeastern Pacific in CMIP5. The intermodel differences suggest considerable model uncertainty in some areas heavily impacted by ARs (e.g., California, Chile), although natural variability is an important factor to consider when interpreting these intermodel differences because the analysis period (i.e., 24 years) may not be long enough to average out decadal to interannual natural variability. For the zonal IVT, most of the areas of considerable systematic bias and larger standard deviation about the bias occur in the tropics (Figures 3e and 3f), where the frequency of ARs is considerably smaller and thus will not be elaborated on more here. For the meridional IVT, there is a clear systematic bias in the simulations; namely, the poleward AR transports are too weak by ~25% (Figures 3g and 3i).

3.4. Intermodel Differences in Future Projections

Figure 4 is similar in layout to Figure 3, although in this case it reflects the difference between the RCP8.5 and historical simulations (i.e., projected changes), as opposed to the difference between the historical simulation and reanalysis (i.e., biases); thus, it shows elements of model agreement across their projected changes in ARs. Figure 4a represents similar information as Figure 2f (i.e., AR frequency mean change) with a different color scale, with Figures 4b and 4c indicating that the greatest intermodel difference in the projected AR frequency changes is in the midlatitudes (~ ±2% and ±4% for Northern and Southern Hemispheres, respectively) where the highest changes in AR frequency occur (~5% and 10% for Northern and Southern Hemispheres, respectively). In these regions, the magnitude of the intermodel differences is roughly 40% of the multimodel ensemble mean. Based on the Community Earth System Model large ensemble, Hagos et al. (2016) estimated natural variability, represented by one standard deviation of the individual ensemble members, to contribute 23% uncertainty in the multimember ensemble mean in projected changes in AR frequency over the western North America from years 1980–1999 to 2080–2099. The much larger model uncertainty shown here (i.e., 40%), represented by one standard deviation across the different models, suggests that natural variability may not fully explain the intermodel differences in projected changes in AR frequency. Figures 4d and 4f show that overall the models uniformly project stronger eastward zonal AR IVT in the midlatitudes, with increases of about 20% in the southern and northern midlatitudes (i.e., compare Figures 3f and 4f). There is a modest weakening of zonal AR IVT in the tropics, particularly the westward transports in the eastern Pacific Ocean—although it is worth noting that this region has very low AR frequency and large intermodel spread. Figures 4g and 4i indicate that the meridional AR export of moisture out of the tropics slightly

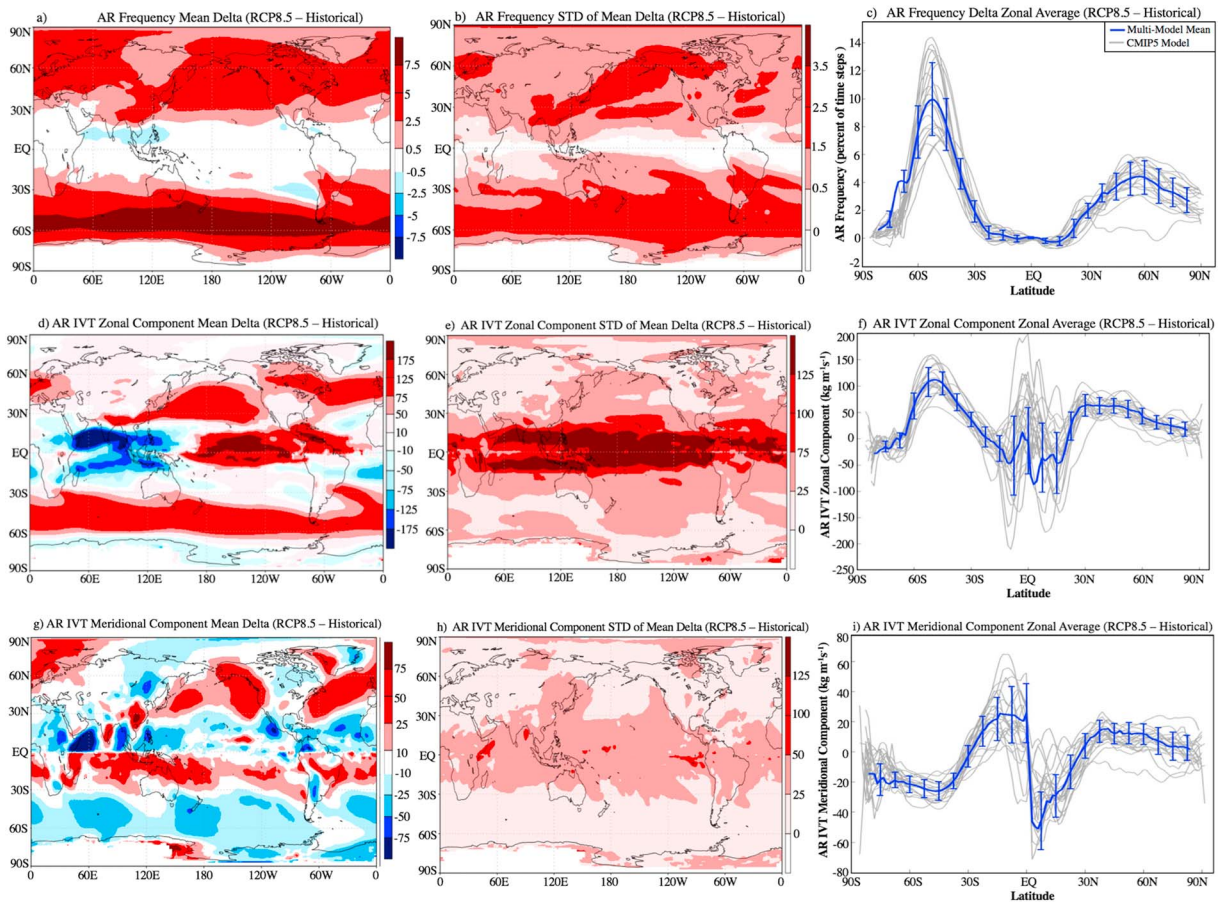


Figure 4. As Figure 3 but for the changes in AR frequency (percent of time steps) and IVT ($\text{kg} \cdot \text{m}^{-1} \cdot \text{s}^{-1}$) between historical and RCP8.5 simulations.

weakens but strengthens considerably in the midlatitudes. Specifically, the projected changes in the mean zonal and meridional AR IVT are about 60 and $10 \text{ kg} \cdot \text{m}^{-1} \cdot \text{s}^{-1}$, respectively, in the northern midlatitudes and 100 and $-25 \text{ kg} \cdot \text{m}^{-1} \cdot \text{s}^{-1}$, respectively, in southern midlatitudes. These results indicate that there is about a 30% projected increase in zonal AR IVT and 5–10% in meridional AR IVT for the RCP8.5 scenario. While Figures 4e and 4h show pronounced intermodel variability in the tropics, it is important to note again that this is a region with very low AR frequency (Figure 3c).

More precise quantitative comparisons of model fidelity and projection uncertainties across the models for a number of regions impacted by ARs are given in Figures S2 and S3. These include California, the U.S. east coast, the UK, and southwestern regions of Africa, Australia, and Chile (see green boxes on Figures 2a and 2e). Notable is the degree that California, the UK, and Chile stand out among these regions in the uncertainty of simulated AR frequency for the historical period and projected changes in AR frequency and IVT.

4. Conclusions

This study represents the first global examination of the climate change impacts on ARs associated with future warming scenarios, based on the application of an AR global detection algorithm (Guan & Waliser, 2015) to outputs from 21 CMIP5 models. AR detection for the historical simulation and future projections (RCP4.5 and RCP8.5) are all based on the IVT 85th percentile derived from the historical simulation. Comparisons between the observational reference and multimodel historical values of AR frequency and IVT show that the MMM represent the reference patterns reasonably well, especially the variation with latitude and dominant zonal asymmetries (Figures 2a, 2b, 3, and S1). The results from the analysis of the projections indicate that for the most part AR frequency and IVT values will increase globally. More specifically, for

the RCP8.5 warming scenario, AR frequency increases by ~50% globally, ~60% in the Southern Ocean, and ~50% in the Northern Hemisphere (Figure 2f). Moreover, in these same regions, the mean magnitude (in terms of IVT of the strongest of events) increases by 25% globally and by 20% in the northern and southern mid-and-high latitudes for RCP8.5 (Figure 2f). Notable are the results that for the RCP8.5 scenario, the number of ARs are projected to decrease slightly by ~10%, yet the ARs will be ~25% longer and ~25% wider, leading to an overall increase in the frequency of AR conditions (i.e., Figure 2f), and exhibit more extreme IVT values (Figure 1b). Moreover, examination of the intermodel difference in projected changes suggests agreement among the models on the general increase in AR frequency globally, and the stronger enhancements to AR frequency and IVT in the midlatitudes, particularly the Southern Ocean (Figures 4, S1, S2, and S3). Previous investigations focused on western North America and Europe, along with a related study on IVT in general (Lavers et al., 2016), have illustrated that thermodynamic response (i.e., moistening) of the atmosphere to the warming dominates, and dynamical effects (e.g., increases in wind speeds) are small. The results reported here for climate change impacts on AR frequency and IVT are generally consistent with previous studies that mainly have focused on western North America and western Europe (a number of which are shown in Table 1). A virtue of the present study is not only highlighting the climate change impacts on ARs beyond these two regions but also providing a means to more soundly compare, given the uniform global data sets and methodology, the projected changes, for example, between two given regions (e.g., western North America and western Europe).

Apart from the general agreement in AR frequency and IVT patterns and values between the multimodel historical simulations and observation reference, there are considerable intermodel variations in terms of AR representation and projected changes that suggest caution in terms of the projected changes to ARs. These warrant additional focused efforts on model evaluation and improvement for AR characteristics. Also notable is that there are a couple of regions that exhibit differences in the sign of the AR frequency change, with a few models projecting decreases in AR frequency in the subtropical Pacific regions near North/South America and the western Pacific (Figures 3, 4, S1, and S2). These are expected to be due to shifts in storm track or subtropical jet features, such as those diagnosed by Hagos et al. (2016), Shields and Kiehl (2016a), and Gao et al. (2016) in their studies for western North America and western Europe sectors, although more in-depth study in these regions is warranted. Overall, the results suggest fairly robust agreement at global scales across the models for the climate change impacts on AR frequency and IVT, relatively good agreement in terms of latitudinal dependencies, and relatively poor agreement at regional scales (Figures 3, 4, S2, and S3).

The intermodel differences in projected AR changes, particularly at regional scales, may not be fully explained by natural variability. Better constraining these models in terms of their AR projections is needed given the large societal impacts of these storms. Further works on field experiments, process studies, and model evaluation and improvement (e.g., Guan & Waliser, 2017; Hagos et al., 2015; Payne & Magnusdottir, 2015; Ralph et al., 2016; Wick et al., 2013) need to be undertaken to improve the model fidelity and reduce the uncertainty in the projections.

References

- Dettinger, M. (2011). Climate change, atmospheric rivers, and floods in California—A multimodel analysis of storm frequency and magnitude changes. *Journal of the American Water Resources Association*, 47(3), 514–523. <https://doi.org/10.1111/j.1752-1688.2011.00546.x>
- Dettinger, M. D. (2013). Atmospheric rivers as drought busters on the U.S. West Coast. *Journal of Hydrometeorology*, 14(6), 1721–1732. <https://doi.org/10.1175/JHM-D-13-02.1>
- Dettinger, M. D., Ralph, F. M., Das, T., Neiman, P. J., & Cayan, D. R. (2011). Atmospheric rivers, floods, and the water resources of California. *Water*, 3(2), 445–478. <https://doi.org/10.3390/w3020445>
- Gao, Y., Lu, J., Leung, L. R., Yang, Q., Hagos, S., & Qian, Y. (2015). Dynamical and thermodynamical modulations on future changes of landfalling atmospheric rivers over western North America. *Geophysical Research Letters*, 42, 7179–7186. <https://doi.org/10.1002/2015GL065435>
- Gao, Y., Lu, J., & Leung, R. (2016). Uncertainties in projecting future changes in atmospheric rivers and their impacts on heavy precipitation over Europe. *Journal of Climate*, 29(18), 6711–6726. <https://doi.org/10.1175/JCLI-D-16-0088.1>
- Gorodetskaya, I. V., Tsukernik, M., Claes, K., Ralph, M. F., Neff, W. D., & Van Lipzig, N. P. M. (2014). The role of atmospheric rivers in anomalous snow accumulation in East Antarctica. *Geophysical Research Letters*, 41, 6199–6206. <https://doi.org/10.1002/2014GL060881>
- Guan, B., Molotch, N. P., Waliser, D. E., Fetzer, E. J., & Neiman, P. J. (2010). Extreme snowfall events linked to atmospheric rivers and surface air temperature via satellite measurements. *Geophysical Research Letters*, 37, L20401. <https://doi.org/10.1029/2010GL044696>
- Guan, B., & Waliser, D. E. (2015). Detection of atmospheric rivers: Evaluation and application of an algorithm for global studies. *Journal of Geophysical Research: Atmospheres*, 120, 12,514–12,535. <https://doi.org/10.1002/2015JD024257>

Acknowledgments

We acknowledge the World Climate Research Programme's Working Group on Coupled Modeling, which is responsible for CMIP, and we thank the climate modeling groups for producing and making available their model output. For CMIP the U.S. Department of Energy's Program for Climate Model Diagnosis and Intercomparison provides coordinating support and lead development of software infrastructure in partnership with the Global Organization for Earth System Science Portals. The ERA-Interim reanalysis data set is available via <http://apps.ecmwf.int/datasets/data/interim-full-daily/>, and the CMIP5 model output data are available via https://cmip.lnl.gov/cmip5/data_portal.html. This research was supported by the NASA Energy and Water cycle Study (NEWS) program. DEW's contribution to this study was carried out on behalf of the Jet Propulsion Laboratory, California Institute of Technology, under a contract with the National Aeronautics and Space Administration. Vicky Espinoza's contribution to this study was made possible by NASA Jet Propulsion Laboratory's Year-Round Internship Program during her graduate studies at the University of Southern California.

- Guan, B., & Waliser, D. E. (2017). Atmospheric rivers in 20 year weather and climate simulations: A multimodel, global evaluation. *Journal of Geophysical Research: Atmospheres*, 122, 5556–5581. <https://doi.org/10.1002/2016JD026174>
- Hagos, S., Leung, L. R., Yang, Q., Zhao, C., & Lu, J. (2015). Resolution and dynamical core dependence of atmospheric river frequency in global model simulations. *Journal of Climate*, 28(7), 2764–2776. <https://doi.org/10.1175/JCLI-D-14-00567.1>
- Hagos, S. M., Leung, L. R., Yoon, J.-H., Lu, J., & Gao, Y. (2016). A projection of changes in landfalling atmospheric river frequency and extreme precipitation over western North America from the large ensemble CESM simulations. *Geophysical Research Letters*, 43, 1357–1363. <https://doi.org/10.1002/2015GL067392>
- Lavers, D. A., Allan, R. P., Villarini, G., Lloyd-Hughes, B., Brayshaw, D. J., & Wade, A. J. (2013). Future changes in atmospheric rivers and their implications for winter flooding in Britain. *Environmental Research Letters*, 8(3), 034010. <https://doi.org/10.1088/1748-9326/8/3/034010>
- Lavers, D. A., Allan, R. P., Wood, E. F., Villarini, G., Brayshaw, D. J., & Wade, A. J. (2011). Winter floods in Britain are connected to atmospheric rivers. *Geophysical Research Letters*, 38, L23803. <https://doi.org/10.1029/2011GL049783>
- Lavers, D. A., Ralph, F. M., Waliser, D. E., Gershunov, A., & Dettinger, M. D. (2015). Climate change intensification of horizontal water vapor transport in CMIP5. *Geophysical Research Letters*, 42, 5617–5625. <https://doi.org/10.1002/2015GL064672>
- Lavers, D. A., Waliser, D. E., Ralph, F. M., & Dettinger, M. D. (2016). Predictability of horizontal water vapor transport relative to precipitation: Enhancing situational awareness for forecasting western U.S. extreme precipitation and flooding. *Geophysical Research Letters*, 43, 2275–2282. <https://doi.org/10.1002/2016GL067765>
- Leung, L. R., & Qian, Y. (2009). Atmospheric rivers induced heavy precipitation and flooding in the western U.S. simulated by the WRF regional climate model. *Geophysical Research Letters*, 36, L03820. <https://doi.org/10.1029/2008GL036445>
- Neiman, P. J., Ralph, F. M., Wick, G. A., Lundquist, J. D., & Dettinger, M. D. (2008). Meteorological characteristics and overland precipitation impacts of atmospheric rivers affecting the west coast of North America based on eight years of SSM/I satellite observations. *Journal of Hydrometeorology*, 9(1), 22–47. <https://doi.org/10.1175/2007Jhm855.1>
- Neiman, P. J., Schick, L. J., Ralph, F. M., Hughes, M., & Wick, G. A. (2011). Flooding in western Washington: The connection to atmospheric rivers. *Journal of Hydrometeorology*, 12(6), 1337–1358. <https://doi.org/10.1175/2011JHM1358.1>
- Neiman, P. J., White, A. B., Ralph, F. M., Gottas, D. J., & Gutman, S. I. (2009). A water vapor flux tool for precipitation forecasting. *Water Management*, 162(2), 83–94. <https://doi.org/10.1680/wama.2009.162.2.83>
- Payne, A. E., & Magnusdottir, G. (2015). An evaluation of atmospheric rivers over the North Pacific in CMIP5 and their response to warming under RCP 8.5. *Journal of Geophysical Research: Atmospheres*, 120, 11,173–11,190. <https://doi.org/10.1002/2015JD023586>
- Pierce, D. W., Cayan, D. R., Das, T., Maurer, E. P., Miller, N. L., Bao, Y., et al. (2013). The key role of heavy precipitation events in climate model disagreements of future annual precipitation changes in California. *Journal of Climate*, 26(16), 5879–5896. <https://doi.org/10.1175/JCLI-D-12-00766.1>
- Radić, V., Cannon, A. J., Menounos, B., & Gi, N. (2015). Future changes in autumn atmospheric river events in British Columbia, Canada, as projected by CMIP5 global climate models. *Journal of Geophysical Research: Atmospheres*, 120, 9279–9302. <https://doi.org/10.1002/2015JD023279>
- Ralph, F. M., & Dettinger, M. D. (2011). Storms, floods, and the science of atmospheric rivers. *Eos, Transactions American Geophysical Union*, 92(32), 265. <https://doi.org/10.1029/2011EO320001>
- Ralph, F. M., Neiman, P. J., & Wick, G. A. (2004). Satellite and CALJET aircraft observations of atmospheric rivers over the eastern North Pacific Ocean during the winter of 1997/98. *Monthly Weather Review*, 132(7), 1721–1745. [https://doi.org/10.1175/1520-0493\(2004\)132%3C1721:SACAO%3E2.0.CO;2](https://doi.org/10.1175/1520-0493(2004)132%3C1721:SACAO%3E2.0.CO;2)
- Ralph, F. M., Neiman, P. J., Wick, G. A., Gutman, S. I., Dettinger, M. D., Cayan, D. R., & White, A. B. (2006). Flooding on California's Russian River: Role of atmospheric rivers. *Geophysical Research Letters*, 33, L13801. <https://doi.org/10.1029/2006GL026689>
- Ralph, F. M., Neiman, P. J., Zamora, R. J., & Dettinger, M. D. (2013). Observed impacts of duration and seasonality of atmospheric-river landfalls on soil moisture and runoff in coastal Northern California. *Journal of Hydrometeorology*, 14(2), 443–459. <https://doi.org/10.1175/JHM-D-12-076.1>
- Ralph, F. M., Prather, K. A., Cayan, D., Spackman, J. R., Demott, P., Dettinger, M., & Intrieri, J. (2016). CalWater field studies designed to quantify the roles of atmospheric rivers and aerosols in modulating U.S. West Coast precipitation in a changing climate. *Bulletin of the American Meteorological Society*, 97(7), 1209–1228. <https://doi.org/10.1175/bams-d-14-00043.1>
- Ramos, A. M., Tomé, R., Trigo, R. M., Liberato, M. L. R., & Pinto, J. G. (2016). Projected changes in atmospheric rivers affecting Europe in CMIP5 models. *Geophysical Research Letters*, 43, 9315–9323. <https://doi.org/10.1002/2016GL070634>
- Shields, C. A., & Kiehl, J. T. (2016a). Atmospheric river landfall-latitude changes in future climate simulations. *Geophysical Research Letters*, 43, 8775–8782. <https://doi.org/10.1002/2016GL070470>
- Shields, C. A., & Kiehl, J. T. (2016b). Simulating the pineapple express in the half degree Community Climate System Model, CCSM4. *Geophysical Research Letters*, 43, 7767–7773. <https://doi.org/10.1002/2016GL069476>
- Taylor, K. E., Stouffer, R. J., & Meehl, G. A. (2012). An overview of CMIP5 and the experiment design. *Bulletin of the American Meteorological Society*, 93(4), 485–498. <https://doi.org/10.1175/BAMS-D-11-00094.1>
- Waliser, D. E., & Guan, B. (2017). Extreme winds and precipitation during landfall of atmospheric rivers. *Nature Geoscience*, 10(3), 179–183. <https://doi.org/10.1038/NGEO2894>
- Waliser, D. E., Moncrieff, M., Burridge, D., Fink, A., Gochis, D., Goswami, B. N., et al. (2012). The “Year” of tropical convection (May 2008 to April 2010): Climate variability and weather highlights. *Bulletin of the American Meteorological Society*, 93(8), 1189–1218. <https://doi.org/10.1175/2011BAMS3095.1>
- Warner, M., Mass, C. F., & Salathé, E. P. (2015). Changes in winter atmospheric rivers along the North American west coast in CMIP5 climate models. *Journal of Hydrometeorology*, 16(1), 118–128. <https://doi.org/10.1175/JHM-D-14-0080.1>
- Wick, G. A., Neiman, P. J., Ralph, F. M., & Hamill, T. M. (2013). Evaluation of forecasts of the water vapor signature of atmospheric rivers in operational numerical weather prediction models. *Weather and Forecasting*, 28(6), 1337–1352. <https://doi.org/10.1175/WAF-D-13-00025.1>
- Zhu, Y., & Newell, R. E. (1998). A proposed algorithm for moisture fluxes from atmospheric rivers. *Monthly Weather Review*, 126(3), 725–735. <https://doi.org/10.1175/1520-0493>